



# Depolarization compensation with a spatially variable wave plate in a 116 W, 441 fs, 1 MHz Yb:YAG double-pass laser amplifier

LAURYNAS VESELIS,<sup>1,\*</sup> RAIMUNDAS BUROKAS,<sup>2</sup> ORESTAS ULČINAS,<sup>1,3</sup> TITAS GERTUS,<sup>4</sup> KIRILAS MICHAILOVAS,<sup>2</sup> AND ANDREJUS MICHAILOVAS<sup>1,2</sup> 

<sup>1</sup>Center for Physical Sciences and Technology, Savanoriu Ave. 231, LT-02300, Vilnius, Lithuania

<sup>2</sup>Eksplo Ltd., Savanoriu Ave. 237, LT-02300 Vilnius, Lithuania

<sup>3</sup>Workshop of Photonics, Mokslininku st. 6A, Vilnius LT-08412, Lithuania

<sup>4</sup>Light Conversion, Keramiku st. 2B, LT-10233, Vilnius, Lithuania

\*Corresponding author: lveselis@gmail.com

Received 3 June 2021; revised 13 July 2021; accepted 14 July 2021; posted 14 July 2021 (Doc. ID 432573); published 12 August 2021

**A subpicosecond laser system featuring a fiber chirped pulse amplification-based seed laser and a double-pass end-pumped Yb:YAG crystal power amplifier was investigated. The key novelty of the system was the application of depolarization compensation using a specially designed spatially variable wave plate. To the best of our knowledge, this method was applied for the first time. The presented laser system produced pulses of 441 fs duration, 116  $\mu$ J pulse energy at 116 W average power with a beam quality of  $M^2 \sim 2.1$ , featured optical-to-optical efficiency of 32% at room temperature ( $T = 20^\circ\text{C}$ ), and had residual depolarization level of 2.7%. © 2021 Optical Society of America**

<https://doi.org/10.1364/AO.432573>

## 1. INTRODUCTION

Subpicosecond high peak power ( $\text{TW}/\text{cm}^2$ ) and high repetition rate (megahertz) Yb-doped laser materials-based laser systems are used in various fields of science and industry, such as various materials processing, ultrafast spectroscopy, nonlinear imaging, etc. [1–3]. However, generation of such pulses is a challenge—direct amplification of high peak power subpicosecond pulses is limited by nonlinear effects such as self-phase modulation, self-focusing, Raman scattering, etc. These undesirable and limiting effects are efficiently mitigated with the chirped pulse amplification (CPA) technique [4]. Pulse stretching and compression are usually realized with diffraction grating setups with matched chromatic dispersion profiles [5,6]. However, when pulses are chirped to a few hundreds of picoseconds or longer duration, such CPA systems become impractical due to the size of the required gratings. Fiber-optic seeders and all-in fiber stretchers help in size reduction [7,8]. Still, pulse energy and, therefore, peak power of pulses produced by fiber lasers are limited by the relatively small mode area of single-mode fibers. Higher peak power pulses can be obtained using a cascade of additional free-space solid-state amplifiers.

Ytterbium (Yb)-doped laser crystals (e.g., Yb:YAG, Yb:KYW, Yb:KGW) feature low quantum defect, broad amplification bandwidth, and low excited state absorption, which make them a straightforward choice for building solid-state amplifiers [9–12]. However, reaching high optical-to-optical efficiency at

room temperature requires high peak power pumping due to the quasi-three-level nature of  $\text{Yb}^{3+}$  ions. Cryogenically cooled systems were proposed as a solution, but they add considerable complexity, bulkiness, and cost, which is disadvantageous for industrial applications [13]. The recent introduction of commercially available high-brightness ( $\text{NA} < 0.22$ ) pump diodes enabled a more practical approach [14]. Additionally, double-pass bulk amplifier configuration proved to be an efficient solution for enhanced extraction of power at room temperatures [15].

One of the most efficient Yb-doped materials for application as a laser amplifier is the Yb:YAG crystal, featuring high absorption and amplification cross sections and high thermal conductivity. Though Yb-doped materials have a quite small quantum defect when pumped by 969 nm laser diodes, thermal effects in the highly pumped gain medium cause significant power losses via depolarization if a laser system contains polarization-sensitive elements (e.g., Brewster plates, Faraday rotators, polarizers). In the end-pumped geometry and side cooling of such a medium, a characteristic temperature distribution with its maximum in the center of the element (coincides with pumping region) and minimum at the medium boundary, results in axially symmetric temperature gradients. These gradients induce mechanical stresses in pumped crystal, which lead to correlated to gradient distribution of refractive indices and induced birefringence [16]. For [111]-cut Yb:YAG crystals,

birefringence axes are oriented in the radial and tangential directions to the gradient field (crystal axis of symmetry), leading to a common “clover leaf” depolarized beam shape of initially linearly polarized light at the input of the amplifier [17]. Thermally induced stresses not only affect spatial beam profile but result in bifocusing, which spoils beam focusability [18]. Many techniques for mitigating problems related to thermal stress have been proposed. For optically isotropic gain media such as Yb:YAG, depolarization loss can be minimized by using the classic depolarization compensation layout of two identical laser modules that are placed one after another, employing polarization rotation and relay imaging between them [19]. The basic idea of such compensation methods is to inverse polarization states across the beam profile before entering the second active element and, in this way, equalize accumulated phase difference between radial and tangential polarization. Some research was performed for different crystal cut directions demonstrating reduction of depolarization level in Yb:YAG and Nd:YAG crystals [20–22]. Furthermore, a relatively simple technique for reducing the depolarization loss was demonstrated, employing a single intracavity quarter-wave plate with its fast or slow axis aligned parallel to the preferred plane of polarization [23,24]. Significant compensation of depolarization and bifocusing in laser rods by employing an intracavity Faraday rotator was also demonstrated [25]. All these methods work to some extent; however, posing some serious drawbacks—either depolarization is not fully compensated in the highly pumped gain medium [24], is susceptible to thermal effects, as is the case with Faraday rotators due to relatively strong absorption of laser radiation of the magneto-optical material [26], suffers from nonlinear interaction due to large nonlinear refractive index of the magneto-optical material (leading to self-focusing, spectrum modulation, beam quality degradation) [25,26], requires precise alignment and similar pumping conditions [19,24,25]—or is somewhat too sensitive to crystal configuration and alignment (different cut crystals).

If depolarization problems for the end-pumped Yb:YAG amplifier are solved, due to its simplicity, it would be preferable geometry compared to other geometries, e.g., thin disk or crystal fiber [27,28]. A crystal fiber-based amplifier [29] is usually arranged in a double-pass configuration for signal beam, whereas pump radiation propagates in the single-pass regime. Due to the high surface-to-volume ratio, crystal fiber provides means for excellent thermal management, but still suffers from depolarization losses. On the other hand, thin disk geometry is less sensitive to depolarization losses; however, it requires multipass amplification arrangements due to relatively short gain length.

These reasons motivated us to search for a novel yet practical approach to reducing depolarization and bifocusing in a highly end-pumped gain medium to build a more efficient high peak power subpicosecond laser system. A very promising technology, which allows mimicking birefringence of thermally stressed Yb:YAG crystals, is the inscription of nanogratings in optically transparent materials, e.g., fused silica [30–33]. The choice of such material as the substrate for the depolarization compensator is beneficial for two main reasons. First, low bulk absorption of fused silica [34] avoids degrading thermal effects, as is the case with Faraday rotators [26]. Second, nonlinear

interaction in high-intensity lasers is minimized compared to the Faraday rotator case due to a significantly lower nonlinear refractive index of fused silica [35,36]. Additionally, a fused silica substrate of 6 mm is used, whereas Faraday rotator typical material length is 20 mm [36], substantially reducing nonlinear interaction length.

The formation of self-assembled periodic subwavelength structures (“nanogratings”) in a volume of bulk fused silica glass has been announced as one of the breakthroughs in photonics [37]. These modifications exhibit optical anisotropy with controllable birefringence, allowing the fabrication of different unique optical elements. Worth mentioning are S-wave plates, linear-to-radial or azimuthal polarization converters, birefringent phase gratings and holograms, rewritable 5D optical memory, spatial beam formation tools, and many others, all exhibiting the high damage threshold of bulk fused silica glass [38,39]. The main feature of these nanogratings is that, by choosing a certain parameter range of femtosecond laser, one can precisely point-by-point inscribe oriented birefringence in the volume of transparent material featuring no absorption and very low scattering [40]. Knowledge of depolarization level in Yb:YAG laser amplifier, its origin, and amplified laser beam parameters (shape and initial polarization state) would allow using such fabricated element (spatially variable wave plate or SVWP) as an efficient and practical depolarization compensator.

In this paper, we present an approach to building a high peak power subpicosecond laser system utilizing a hybrid laser concept. As a system seed source, a modified version of fiber CPA-based FemtoLux 30 laser (*Ekspla*, Lithuania) was used [8,15]. For further power scaling, a double-pass end-pumped Yb:YAG power amplifier configuration was employed with a novel approach of depolarization compensation using SVWP. Finally, amplified pulses were efficiently compressed in a diffraction-grating-based four-pass pulse compressor.

## 2. THEORY AND NUMERICAL INVESTIGATION OF SVWP ELEMENT

An end-pumped Yb:YAG crystal in a power amplifier layout introduces wavefront and polarization distortions in an initially near-ideal Gaussian beam profile. In this section, we present results of modeling of the proposed polarization distortions compensator, targeted to enhance polarization state and reduce astigmatism of the amplified beam.

### A. SVSP Model

SVWPs can be designed for incident beams with either linear or circular polarization. In both cases, a continuously varying fast axis orientation of nanogratings is constructed and aligned by axis in the tangential direction, as is shown in Fig. 1. A radially varying retardance value is continuously formed at each point. Phase retardance  $\delta$  can be expressed as

$$\delta(r) = \frac{\lambda}{2} \left( \frac{r}{R} \right)^2, \quad (1)$$

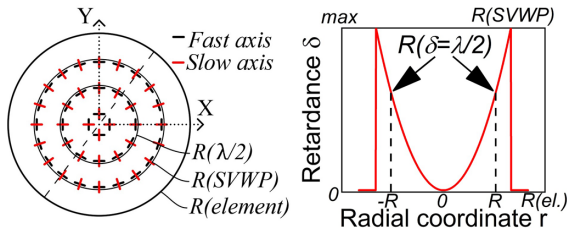


**Fig. 1.** Left: two-dimensional fast and slow axis orientation distribution map.  $R(\lambda/2)$  marks the contour of SVWP where phase retardance is  $\lambda/2$ ,  $R(\text{SVWP})$  marks the edge of the inscribed birefringence map, and  $R(\text{el.})$  marks the radius of the glass substrate of the element. Right, retardance profile across the dashed line within SVWP element.

where  $\lambda$  is the wavelength,  $r$  is the radial coordinate, and  $R$  is the radial coordinate of an element where phase retardance reaches a value of  $\lambda/2$ .

$$E = \begin{pmatrix} \cos \beta E_{0x} \left( \cos^2 \theta + e^{-i\frac{2\pi}{\lambda} \delta} \sin^2 \theta \right) + \sin \beta E_{0y} e^{i\Delta\varphi} \left( \sin \theta \cos \theta - e^{-i\frac{2\pi}{\lambda} \delta} \sin \theta \cos \theta \right) \\ \cos \beta E_{0x} \left( \sin^2 \theta \cos \theta - e^{-i\frac{2\pi}{\lambda} \delta} \sin \theta \cos \theta \right) + \sin \beta E_{0y} e^{i\Delta\varphi} \left( \sin^2 \theta + e^{-i\frac{2\pi}{\lambda} \delta} \cos^2 \theta \right) \end{pmatrix}. \quad (2)$$

Following Jones matrix formalism, the SVWP element can be expressed as a phase retarder with arbitrary retardation along the radial and the tangential axis [17,41]. A polarized electric field that passed this element is then defined as shown in Eq. (2), where  $E_{x0}$ ,  $E_{y0}$  are input electric fields in the horizontal and the vertical plane,  $\theta$  is the angle between reference polarization axis and local birefringence axis,  $\beta$  is the angle of linearly polarized light with respect to the horizontal plane ( $x$  axis),  $\Delta\varphi$  is the phase difference between electric fields in the horizontal and the vertical plane, and  $\delta$  is the induced phase retardance between polarization components. Such parabolic birefringence distribution in SVWP mimics the thermally induced birefringence in the end-pumped gain medium [42]. In theory, if the birefringence profile is inverted in SVWP, it would be capable of

compensating thermally induced depolarization and bifocusing in the pumped gain medium.

## B. Peculiarities of SVWP Element

In this section, we present numerical results of the performance of the SVWP element designed for depolarization compensation. The case when linear or circular input Gaussian beam polarization propagates through the SVWP element was investigated. Depolarization level  $\eta$  dependence on the phase retardance  $\delta$  induced by the SVWP element was calculated and presented in Fig. 2 (bottom graph). The ratio of beam radius to compensator radius  $r/R$  required to compensate for the induced phase retardance is plotted in Fig. 2 (top). Few cases of required  $r/R$  ratio for different retardance  $\delta$  values are displayed as a reference. Analytical expressions to calculate required

parameters of SVWP for certain depolarization values for ideal Gaussian beam are depicted too. It is important to note that depolarization for circular polarization case is 2 times larger than for linear polarization with the same phase retardance, but the required compensation ratio  $r/R$  stays the same.

Another aspect of the SVWP element is the intrinsic astigmatism that it produces for the linearly polarized beam passing through it, or the symmetrical focusing induced for the circularly polarized beam. Modeling was performed by propagating the ideal Gaussian beam through SVWP using the Fourier transform method and Eq. (2) and calculating the resulting beam wavefront radius. Modeling results indicate that every percent of deviation in inscribed phase retardance from the design

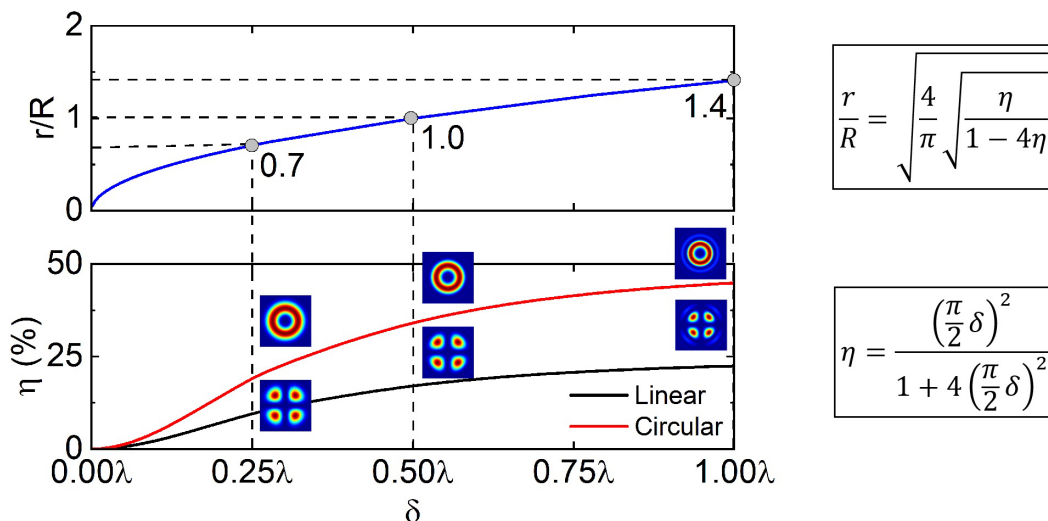


**Fig. 2.** Top, the ratio of beam radius to compensator radius  $r/R$  required for compensation of induced phase retardance by SVWP element; bottom, beam depolarization level dependence on induced phase retardance by SVWP element. Dashed lines indicate the values of ratio  $r/R$  required to compensate for corresponding phase retardance in a laser beam. Insets, depolarized beam profiles for circular (top) and linear (bottom) polarization at different phase retardance induced by SVWP element. Corresponding analytical expressions for linear polarization cases are provided, based on derivations from [21].

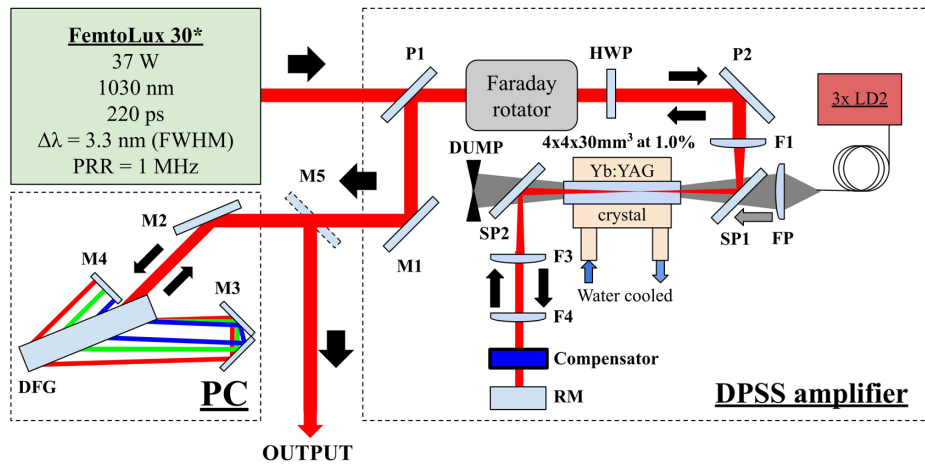


**Fig. 3.** Layout of the developed laser system consisting of CPA-based customized laser FemtoLux 30 as a seed source, DPSS Yb:YAG power amplifier, and four-pass diffraction grating pulse compressor. LD2, CW laser diode (CWL 940 nm, 130 W, NA = 0.22, D = 200  $\mu\text{m}$ ; set of three diodes used, coupled via fiber combiner); HWP, half wave plate; F1, focusing lens system to Yb:YAG crystal; P1, P2, polarizers; SP1, SP2, signal and pump beam separating mirrors; F3 and F4, pair of focusing lenses for thermal lensing compensation; RM, flat mirror for beam backreflection; FP, pump beam focusing optics; DUMP, beam block of unabsorbed pump radiation after a single pass; M1, M2, mirrors; M3, mirror pair for pulse compressor optical path folding; M4, mirror for beam returning in pulse compressor; M5, output mirror; DFG, diffraction grating with 1739  $\text{mm}^{-1}$  groove density; PC corresponds to a four-pass diffraction grating-based pulse compressor.

value translates to the same amount of uncompensated bilens power. For example, if we take  $r = 1$  mm, and  $R = 1$  mm for the initially linearly polarized beam, the bilens power produced by SVWP would be  $D = 1.03$   $\text{m}^{-1}$ . If the SVWP element compensates for the depolarization as designed, but with the error of 5%, uncompensated lensing power would be  $D = 0.05$   $\text{m}^{-1}$  (or  $F = 20$  m). Moreover, an increase of beam size reduces absolute lensing sensitivity by the power of 2 (whereas compensated depolarization sensitivity drops linearly). This suggests that it is practical to have a relatively large beam passing through the SVWP element.

### 3. EXPERIMENTAL RESULTS AND DISCUSSION

Experimental setup of subpicosecond high peak power and high repetition rate (megahertz) laser system is seeded by a prototype version of the *FemtoLux 30* laser (*Ekspla*, Lithuania), featuring output power of 37 W at 1 MHz pulse repetition rate, pulses chirped to  $\sim 220$  ps duration, and bandwidth of  $\Delta\lambda = 3.3$  nm (at FWHM), centered at 1030 nm. The full laser system layout is shown in Fig. 3.

The output beam from the seed laser of nearly Gaussian shape was collimated to a 2 mm diameter beam (at  $1/e^2$  level). Beam quality was characterized using the standard  $z$ -scan technique by focusing the beam using a positive lens of well-defined focal length and tracing the beam radius change along the propagation direction. The best fit to  $z$  scan yielded  $M^2 \sim 1$ , indicating nearly diffraction-limited beam quality, as shown in Fig. 4.

To estimate seed pulse quality prior to amplification in a two-pass diode-pumped solid-state (DPSS) Yb:YAG amplifier, seed pulses were compressed in a four-pass diffraction grating compressor, with 1739  $\text{mm}^{-1}$  groove density diffraction grating (as is shown in Fig. 3). Compressed pulses were characterized by the second-harmonic generation frequency-resolved optical

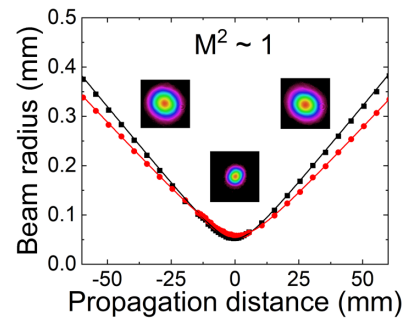


**Fig. 4.** Beam radius measurement along focused beam direction at the output of seed source traced via  $z$ -scan technique (dots). Beam quality parameter  $M^2 \sim 1$  was estimated from the fit (curves). Images of the beam profile at a few positions are shown as insets (beam size was normalized for clarity).

generating (SHG-FROG) autocorrelation method. The pulse duration retrieved by the FROG algorithm (Swamp Optics) using a  $1024 \times 1024$  grid was 318 fs (Fig. 5). Bandwidth-limited pulse duration derived from the measured output spectrum was calculated to be 315 fs, indicating a good compressed pulse quality. A residual spectral phase retrieved from FROG was  $\sim 1.6$  rad in the spectral range from 1021.5 to 1033.8 nm, encompassing 98% of total pulse energy. The temporal Strehl ratio of the compressed pulse, defined as the ratio of actual peak power of the pulse to the bandwidth-limited pulse, was 83%, indicating high seed-pulse quality.

Chirped seed pulses were then directed to the DPSS Yb:YAG double-pass amplifier stage. A Yb:YAG crystal (Yb<sup>3+</sup> concentration 1.0%, rod length 30 mm) was mounted into a water-cooled copper block, with high thermal conductivity silicone as a thermal interface between gain medium and heat sink. The temperature of circulating water was set to  $T = 20^\circ\text{C}$ . The input

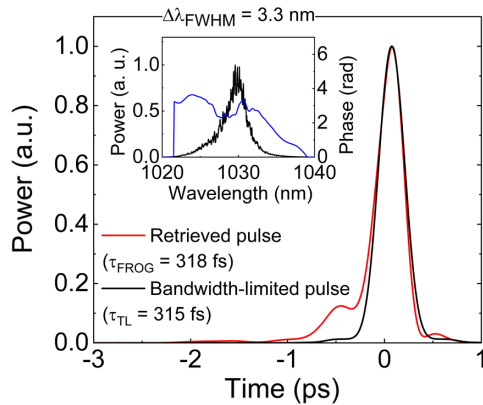


**Fig. 5.** Envelope of the compressed pulses at the output of the seed laser, retrieved from SHG-FROG measurement compared to bandwidth-limited pulse shape calculated from the measured spectrum. Inset, measured amplified signal spectrum and retrieved spectral phase. FROG traces retrieval error was 0.15%. The estimated temporal Strehl ratio of the pulse was 83%.

and output beams of the double-pass amplifier were decoupled via polarization using a half-wave plate (HWP), Faraday rotator, and a pair of polarizers (P1 and P2), as shown in Fig. 3. The Yb:YAG crystal rod was end-pumped by a continuous-wave laser diode. Three identical pumping diodes (output power 130 W, *nLight*), each coupled to 105  $\mu\text{m}$  core diameter and 0.22 numerical aperture (NA) fiber, were combined using a high-power fiber combiner (*ITF Technologies*), featuring 200  $\mu\text{m}$  core diameter and 0.22 NA output. The maximum measured pump power was 280 W at the 940 nm central wavelength featuring 3.5 nm bandwidth (FWHM). Each diode block was placed on the water-cooled heat sink, with temperatures adjusted to center output wavelength at 940 nm (diodes were not wavelength-stabilized). Seed and pump beams were focused by F1 and FP lenses to spots of 0.83 mm and 0.78 mm diameters, respectively, and overlapped in the amplifier crystal (Fig. 3). Unabsorbed pump power was separated from the seed beam by SP2 wavelength separator and dumped. The seed beam was directed by a separator to a lens pair of the focal lengths  $F3 = 75$  mm and  $F4 = 200$  mm. Lens F3 was placed at the focal distance from the crystal, whereas lens F4 was placed at 155 mm distance from lens F3 to compensate for the thermal lens of end-pumped Yb:YAG crystal and to collimate the amplified seed beam after lens F4. Back reflector RM was installed at a focal distance from lens F4. The beam was imaged back to amplifier crystal and outcoupled by polarizer P1 after the second pass (Fig. 3). Dependences of two-pass amplification, pump absorption, and depolarization level on seed power were measured. Results are displayed in Fig. 6 and in Fig. 7.

The maximum output power of 129 W at 1 MHz pulse repetition rate was achieved at 37 W seed power (Fig. 6). For 280 W pump power, it corresponded to 32% amplifier efficiency. At low seed power, 16.7 dB gain was achieved. In Fig. 7 (bottom-right graph), the dependence of depolarization change at different input seed power levels is plotted. At the small-signal gain regime, the depolarization level was 4.2%, and at 37 W input power depolarization level reached 17.9%. It is interesting that the depolarization level depends on input seed power. Such dependence could be explained as follows. As can be seen in

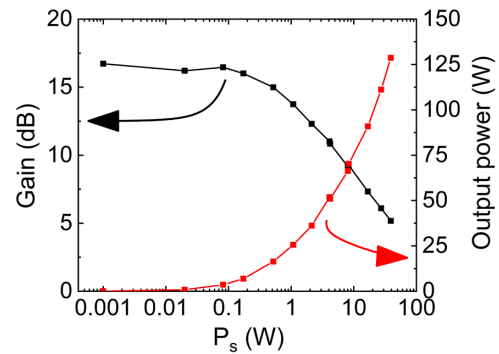


**Fig. 6.** Average output power (red) and total amplifier gain (black) dependence on input seed power in the two-pass amplifier at 280 W pump level.

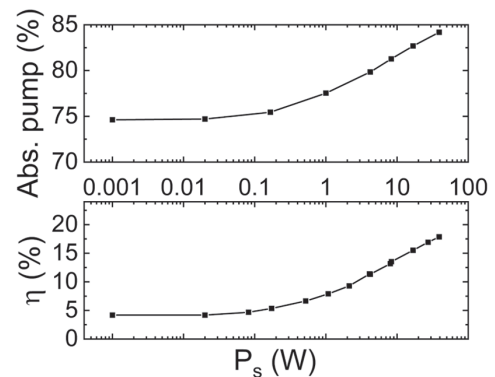


**Fig. 7.** Absorbed pump and induced depolarization  $\eta$  dependence on input seed power in the two-pass amplifier at 280 W pump level.

Fig. 7 (top-right graph), absorbed pump power is dependent on input seed power too. It correlates well with induced depolarization level: when absorbed pump power increases, induced depolarization level also increases. Considerable  $\text{Yb}^{3+}$  upper-state manifold depletion happens at high-input seed power, leading to an increase of pump power absorption, as is the case in both, three- and four-level gain materials. Increased pump absorption results in increased heat generation due to quantum defect and depolarization level increase, since the change in temperature gradients leads to the change in induced depolarization due to the photoelastic effect. Beam profile modification is the second factor that could influence increased depolarization levels. Considerable amplification saturation at high-input seed power leads to different effective gain across beam profile; wings of Gaussian input beam are amplified relatively better than the central lobe, resulting in beam intensity distribution flattening [18]. Additionally, thermal aberrations of the end-pumped gain medium also influence beam intensity redistribution. Beam profile deviation from the Gaussian one, when more power is redistributed into the wings of the Gaussian beam, leads to increased depolarization level, as phase retardance created by the end-pumped gain medium increases parabolically from the center of the beam (Fig. 1 right graph illustrates this).

The spatially variable wave plates for depolarization compensation were designed for several maximum retardances. As the law of retardance is parabolic, it is possible to get different values of total retardance by combining elements with different

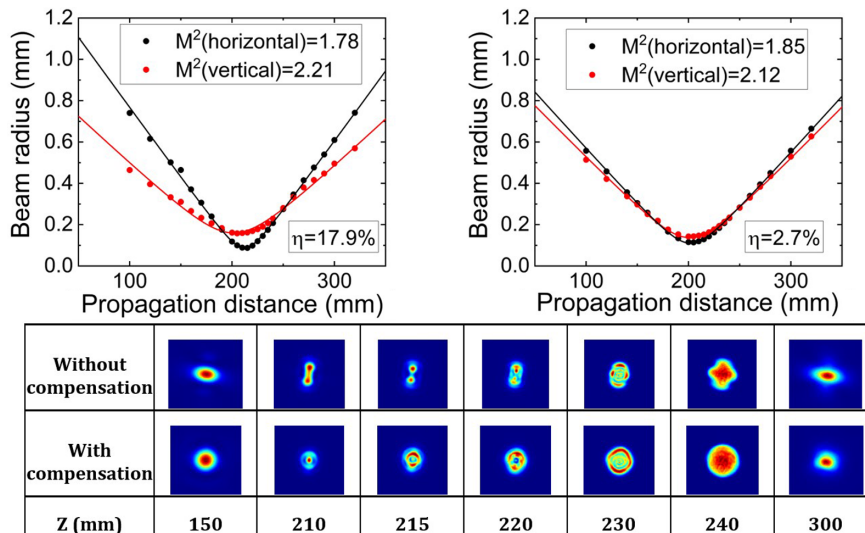


**Fig. 8.** Z scan of the amplified beam without (left) and with (right) depolarization compensation by SVWP compensator. Beam quality parameter  $M^2$  was estimated from the fit (red and black curves),  $M^2 = 1.8$  and  $M^2 = 2.2$  for horizontal and vertical projections of cross section, correspondingly. Images of the beam cross-sectional profiles at several positions along the propagation axis are shown in the table below.

maximum retardances. Additionally, due to the same parabolic retardance profile, by changing the seed beam diameter incident on the SVWP element, we could change the phase retardance induced by the SVWP element, thus adjusting to different pumping conditions. This approach is convenient for experimental flexibility to compensate for a different amount of depolarization in different experimental layouts. A set of SVWP with maximum retardances of  $\lambda/2$ ,  $\lambda/4$ ,  $\lambda/8$ ,  $\lambda/16$ , and  $\lambda/32$  for the central wavelength of 1030 nm was fabricated in fused silica (UVFS) glass substrate by the femtoLAB micromachining system (*Workshop of Photonics*, Lithuania).

SVWP with retardance value of  $\delta = 0.44\lambda$  (at  $R = 1.5$  mm) was used to compensate for the depolarization and bifocusing arising in the double-pass configuration. It was placed near the back reflector RM, as shown in Fig. 3. Initially, the depolarization compensator was removed to check how Yb:YAG amplifier crystal modifies the beam spatial and polarization properties. Z-scan measurement of the amplified beam was performed. The signal beam was focused by  $F = 200$  mm lens placed at 1 m distance from polarizer P1, and beam radius (at 4-sigma level) along the focused beam caustic (z-scan profile) was captured by a CMOS camera. The same procedure was repeated with a depolarization compensator installed. Results of the z scan with and without depolarization compensation in the double-pass amplifier configuration are shown in Fig. 8.

Depolarization level was reduced from 17.9% to 2.7%, and the bifocusing term was minimized to the level we were unable to measure with the depolarization compensator installed. The resulting depolarization compensation and bifocusing reduction were significant due to the correct choice of compensator parameters, saving a lot of output power and preserving symmetrical beam shape. There were several reasons for residual uncompensated depolarization. The first, when pump power was switched off, the “cold” depolarization in the system was around 0.5% due to the stress induced by the crystal mount. The second, a small amount of uncompensated depolarization

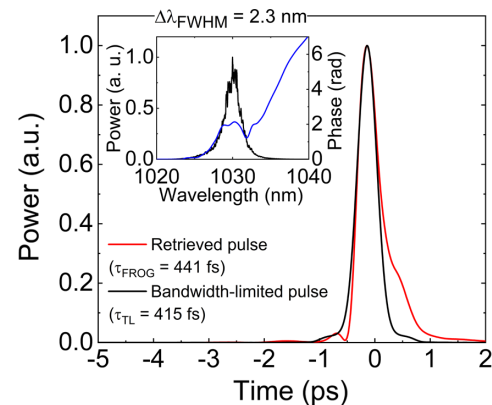


**Fig. 9.** Envelope of the compressed pulses at the output of the two-pass amplifier, retrieved from SHG-FROG measurement compared to bandwidth-limited pulse shape calculated from the measured spectrum. Inset, (left) measured amplified signal spectrum and retrieved spectral phase. FROG traces retrieval error was 0.15%. The estimated temporal Strehl ratio of the pulse was 81%.

could arise due to the manufacturing errors of the SVWP element itself. The third, maximum phase retardation inscribed in the SVWP of 4 mm diameter, was not enough for full compensation of induced depolarization. The compensation could be enhanced by adding one more SVWP in which a small amount of phase retardance is inscribed. As phase retardation could be summed up, the set of several SVWPs could serve any heat load to an amplifier crystal.

Beam quality parameter degradation in the double-pass configuration was severe, resulting in  $M^2 = 1.9–2.2$ , mainly due to thermal aberrations arising in the end-pumped Yb:YAG crystal and gain saturation. Improvement of resulting beam quality is possible and planned in the future.

Pulses were compressed in a four-pass diffraction grating pulse compressor after amplification in a double-pass Yb:YAG amplifier. Temporally compressed pulses were characterized

using the same SHG-FROG method. The measured pulse duration was 441 fs (Fig. 9). Transform-limited pulse duration derived from the output spectrum was 415 fs. A residual spectral phase retrieved from FROG was  $\sim 2.3$  rad in the spectral range from 1024.3 to 1033.8 nm, encompassing 98% of total pulse energy. The temporal Strehl ratio of the compressed pulse, defined as the ratio of actual peak power of the pulse to the one of the bandwidth-limited pulse, was 81%, indicating high amplified pulse quality. Pulse quality minimally degraded compared to an initial seed pulse temporal Strehl ratio of 83%, whereas the pulse bandwidth narrowed from 3.3 nm (at FWHM) to 2.3 nm (at FWHM) due to the gain narrowing effect. Measured diffraction and reflection losses in pulse compressor were  $\sim 10\%$ , resulting in total output power of  $\sim 116$  W, whereas beam quality did not degrade further and remained at  $M^2 = 1.9\text{--}2.2$ .

#### 4. SUMMARY

In this work, a subpicosecond laser system was investigated, featuring fiber CPA-based seed laser FemtoLux 30 (*Ekspla*) and a double-pass end-pumped Yb:YAG crystal power amplifier. The key novelty of the system was the application of depolarization compensation using a specially designed SVWP, which allowed the extraction of nearly maximum power from such an amplifier without additional beam quality degradation. To the best of our knowledge, this method has been applied for the first time. In our opinion, our proposed method is more beneficial compared to others, such as intracavity quarter-wave plate [23,24], intracavity Faraday rotator [25], classical depolarization compensation layout with two identically pumped and relay-imaged gain media [19], and different crystal cut directions [20–22]. The reasons are: (1) the substrate of SVWP is fused silica, providing low bulk absorption of laser radiation and featuring a significantly lower nonlinear refractive index, as compared to a Faraday rotator, thus minimizing thermal effects and nonlinear interaction in high-intensity lasers; (2) the SVWP element is compact (6 mm in thickness, usually 25.4 mm in diameter), whereas Faraday rotator material is usually at least 20 mm in length; (3) there is the possibility to compensate for depolarization in the highly pumped gain medium, which is not the case using a simple approach with a quarter-wave plate, (4) it is not overly sensitive to alignment and specific configuration; (5) it is very practical, as induced/compensated depolarization level can be tuned by either changing the incident laser beam size or stacking a few SVWPs in the same optical layout.

The presented laser system produced pulses of 441 fs duration, 116  $\mu$ J pulse energy at 116 W average power, with a beam quality of  $M^2 \sim 2.1$ , featured optical-to-optical efficiency of 32% at room temperature ( $T = 20^\circ\text{C}$ ), and residual depolarization level of 2.7%. Future work for beam quality improvement is planned.

**Funding.** LVPA (01.2.1-LVPA-K-856-01-0027).

**Disclosures.** The authors declare no conflicts of interest.

**Data Availability.** No data were generated or analyzed in the presented research.

#### REFERENCES

1. L. Shah, M. E. Fermann, J. W. Dawson, and C. P. J. Barty, "Micromachining with a 50 W, 50  $\mu$ J, subpicosecond fiber laser system," *Opt. Express* **14**, 12546–12551 (2006).
2. J. Squier and M. Müller, "High resolution nonlinear microscopy: a review of sources and methods for achieving optimal imaging," *Rev. Sci. Instrum.* **72**, 2855–2867 (2001).
3. R. Berera, R. van Grondelle, and J. T. M. Kennis, "Ultrafast transient absorption spectroscopy: principles and application to photosynthetic systems," *Photosynth. Res.* **101**, 105–118 (2009).
4. D. Strickland and G. Mourou, "Compression of amplified chirped optical pulses," *Opt. Commun.* **56**, 219–221 (1985).
5. E. B. Treacy, "Optical pulse compression with diffraction gratings," *IEEE J. Quantum Electron.* **5**, 454–458 (1969).
6. O. E. Martinez, J. P. Gordon, and R. L. Fork, "Negative group-velocity dispersion using refraction," *J. Opt. Soc. Am. A* **1**, 1003–1006 (1984).
7. G. Imeshev, I. Hartl, and M. E. Fermann, "Chirped pulse amplification with a nonlinearly chirped fiber Bragg grating matched to the Treacy compressor," *Opt. Lett.* **29**, 679–681 (2004).
8. T. Bartulevicius, S. Frankinas, A. Michailovas, R. Vasilyeu, V. Smirnov, F. Trepanier, and N. Rusteika, "Compact fiber CPA system based on a CFBG stretcher and CVBG compressor with matched dispersion profile," *Opt. Express* **25**, 19856–19862 (2017).
9. I. Kuznetsov, I. Mukhin, O. Palashov, and K.-I. Ueda, "Thin-rod Yb:YAG amplifiers for high average and peak power lasers," *Opt. Lett.* **43**, 3941–3944 (2018).
10. J. Pouysegur, M. Delaigue, C. Hönninger, P. Georges, F. Druon, and E. Mottay, "Generation of 150-fs pulses from a diode-pumped Yb:KYW nonlinear regenerative amplifier," *Opt. Express* **22**, 9414–9419 (2014).
11. D. Stučinskas, R. Antipenkov, and A. Varanavičius, "30 W dual active element Yb:KGW regenerative amplifier for amplification of sub-500fs pulses," *Proc. SPIE* **6731**, 67312Y (2007).
12. F. Druon, F. Balembos, and P. Georges, "New materials for short-pulse amplifiers," *IEEE Photon. J.* **3**, 268–273 (2011).
13. D. J. Ripin, J. R. Ochoa, R. L. Aggarwal, T. Y. Fan, and S. Member, "300-W cryogenically cooled Yb:YAG laser," *IEEE J. Quantum Electron.* **41**, 1274–1277 (2005).
14. K. Price, S. Karlsen, P. Leisher, and R. Martinsen, "High-brightness fiber-coupled pump laser development," *Proc. SPIE* **7583**, 758308 (2010).
15. L. Veselis, T. Bartulevicius, K. Madeikis, A. Michailovas, and N. Rusteika, "Compact 20 W femtosecond laser system based on fiber laser seeder, Yb:YAG rod amplifier and chirped volume Bragg grating compressor," *Opt. Express* **26**, 31873–31879 (2018).
16. H. J. Eichler, A. Haase, R. Menzel, and A. Siemoneit, "Thermal lensing and depolarization in a highly pumped Nd:YAG laser amplifier," *J. Phys. D* **26**, 1884–1891 (1993).
17. A. Starobor and O. Palashov, "Peculiarity of the thermally induced depolarization and methods of depolarization compensation in square-shaped Yb:YAG active elements," *Opt. Commun.* **402**, 468–471 (2017).
18. P. Albrodt, X. Delen, M. Besbes, F. Lesparre, and P. Georges, "Simulation and experimental investigation of beam distortions in end-pumped laser rod amplifiers," *J. Opt. Soc. Am. B* **35**, 3004–3013 (2018).
19. K. Michailovas, V. Smilgevičius, and A. Michailovas, "High average power effective pump source at 1 kHz repetition rate for OPCPA system," *Lith. J. Phys.* **54**, 150–154 (2014).
20. D. Albach and J.-C. Chanteloup, "Large size crystalline vs co-sintered ceramic Yb<sup>3+</sup>:YAG disk performance in diode pumped amplifiers," *Opt. Express* **23**, 570–579 (2015).
21. H. Tünnermann, O. Puncken, P. Weßels, M. Frede, D. Kracht, and J. Neumann, "Intrinsic reduction of the depolarization in Nd:YAG crystals," *Opt. Express* **18**, 5496–5501 (2010).
22. H. Tünnermann, O. Puncken, P. Weßels, M. Frede, J. Neumann, and D. Kracht, "Linearly polarized single-mode Nd:YAG oscillators using [100]- and [110]-cut crystals," *Opt. Express* **19**, 12992–12999 (2011).
23. W. A. Clarkson, N. S. Felgate, and D. C. Hanna, "Simple method for reducing the depolarization loss resulting from thermally induced birefringence in solid-state lasers," *Opt. Lett.* **24**, 820–822 (1999).

24. R. Kandasamy, M. Yamanaka, Y. Izawa, and S. Nakai, "Analysis of birefringence compensation using a quarter-wave plate in solid-state lasers," *Opt. Rev.* **7**, 149–151 (2000).
25. M. Ostermeyer, G. Klemz, P. Kubina, and R. Menzel, "Quasi-continuous-wave birefringence-compensated single- and double-rod Nd:YAG lasers," *Appl. Opt.* **41**, 7573–7582 (2002).
26. I. Snetkov, I. Mukhin, O. Palashov, and E. Khazanov, "Compensation of thermally induced depolarization in Faraday isolators for high average power lasers," *Opt. Express* **19**, 6366–6376 (2011).
27. V. Markovic, A. Rohrbacher, P. Hofmann, W. Pallmann, S. Pierrot, and B. Resan, "160 W 800 fs Yb:YAG single crystal fiber amplifier without CPA," *Opt. Express* **23**, 25883–25888 (2015).
28. J. Fischer, A.-C. Heinrich, S. Maier, J. Jungwirth, D. Brida, and A. Leitenstorfer, "615 fs pulses with 17 mJ energy generated by an Yb:thin-disk amplifier at 3 kHz repetition rate," *Opt. Lett.* **41**, 246–249 (2016).
29. F. Li, Z. Yang, Y. Wang, Z. Lv, Q. Li, X. Yang, X. Wang, X. Hu, and W. Zhao, "Hybrid high energy femtosecond laser system based on Yb:YAG single crystal fiber amplifier," *Optik (Stuttgart)* **156**, 155–160 (2018).
30. Y. Shimotsuma, P. G. Kazansky, J. Qiu, and K. Hirao, "Self-organized nanogratings in glass irradiated by ultrashort light pulses," *Phys. Rev. Lett.* **91**, 247405 (2003).
31. S. Richter, M. Heinrich, S. Döring, A. Tünnermann, S. Nolte, and U. Peschel, "Nanogratings in fused silica: formation, control, and applications," *J. Laser Appl.* **24**, 042008 (2012).
32. M. Beresna, M. Gecevičius, and P. G. Kazansky, "Ultrafast laser direct writing and nanostructuring in transparent materials," *Adv. Opt. Photon.* **6**, 293–339 (2014).
33. E. Bricchi, B. G. Klappauf, and P. G. Kazansky, "Form birefringence and negative index change created by femtosecond direct writing in transparent materials," *Opt. Lett.* **29**, 119–121 (2004).
34. F. Nürnberg, B. Kühn, A. Langner, M. Altwein, G. Schötz, R. Takke, S. Thomas, and J. Vydra, "Bulk damage and absorption in fused silica due to high-power laser applications," *Proc. SPIE* **9632**, 96321R (2015).
35. D. Milam, "Review and assessment of measured values of the non-linear refractive-index coefficient of fused silica," *Appl. Opt.* **37**, 546–550 (1998).
36. K. T. Stevens, W. Schlichting, G. Foundos, A. Payne, and E. Rogers, "Promising materials for high power laser isolators," *Laser Tech. J.* **13**, 18–21 (2016).
37. F. Burmeister, S. Richter, D. Richter, C. Voigtlander, A. Heisterkamp, and S. Nolte, "Breakthroughs in photonics 2012: femtosecond-laser nanomachining," *IEEE Photon. J.* **5**, 0700506 (2013).
38. L. Sudrie, M. Franco, B. Prade, and A. Mysyrowicz, "Writing of permanent birefringent microlayers in bulk fused silica with femtosecond laser pulses," *Opt. Commun.* **171**, 279–284 (1999).
39. J. Adamonis, A. Aleknavičius, K. Michailovas, S. Balickas, V. Petruskienė, T. Gertus, and A. Michailovas, "Implementation of a SWWP-based laser beam shaping technique for generation of 100 mJ-level picosecond pulses," *Appl. Opt.* **55**, 8007–8015 (2016).
40. M. Beresna, M. Gecevičius, P. G. Kazansky, and T. Gertus, "Radially polarized optical vortex converter created by femtosecond laser nanostructuring of glass," *Appl. Phys. Lett.* **98**, 201101 (2011).
41. J. J. Morehead, "Compensation of laser thermal depolarization using free space," *IEEE J. Sel. Top. Quantum Electron.* **13**, 498–501 (2007).
42. W. Koechner, *Solid-State Laser Engineering*, Vol. 1 of *Springer Series in Optical Sciences* (Springer, 2006), pp. 406–450.